BNL - 66660

DEVELOPMENTS IN SYNCHROTRON X-RAY COMPUTED MICROTOMOGRAPHY AT THE NATIONAL SYNCHROTRON LIGHT SOURCE

B. A. Dowd, Graham H. Campbell and D. Peter Siddons
Brookhaven National Laboratory
National Synchrotron Light Source
Upton, NY 11973-5000

Robert B. Marr
Department of Applied Science
Brookhaven National Laboratory
National Synchrotron Light Source
Upton, NY 11973-5000

Vivek Nagarkar and Sameer Tipnis
Radiation Monitoring Devices, Inc.
44 Hunt Street
Wartertown, MA 02472

Lisa Axe
New Jersey Institute of Tech.
Dpt. Of Civil & Environmental Eng.
Newark, NJ 07102

July 1999

National Synchrotron Light Source
Operated by
Brookhaven Science Associates
Upton, NY 11973

Under Contract with the United States Department of Energy
Contract Number DE-AC02-98CH10886

DISCLAIMER

Developments in synchrotron x-ray computed microtomography at the National Synchrotron Light Source

Betsy A. Dowd[a*], Graham H. Campbell[a], Robert B. Marr[b], Vivek Nagarkar[c] , Sameer Tipnis[c], Lisa Axe[d], D. Peter Siddons[a]

[a]National Synchrotron Light Source, Brookhaven National Laboratory, Upton, NY 11973
[b]Department of Applied Science, Brookhaven National Laboratory, Upton, NY 11973
[c]Radiation Monitoring Devices, Inc., 44 Hunt Street, Watertown , MA 02472
[d]New Jersey Institute of Tech., Dpt. of Civil & Environmental Eng., Newark, NJ 07102

ABSTRACT

Last year, the X27A beamline at the National Synchrotron Light Source (NSLS) became dedicated solely to X-Ray Computed Microtomography (XCMT). This is a third-generation instrument capable of producing tomographic volumes of 1-2 micron resolution over a 2-3mm field of view. Recent enhancements will be discussed. These have focussed on two issues: the desire for real-time data acquisition and processing and the need for highly monochromatic beam (.1 % energy bandpass). The latter will permit k-edge subtraction studies and will provide improved image contrast from below the Cr (6 keV) up to the Cs (36 keV) k-edge. A range of applications that benefit from these improvements will be discussed as well. These two goals are somewhat counterproductive, however; higher monochromaticity yields a lower flux forcing longer data acquisition times. To balance the two, a more efficient scintillator for X-ray conversion is being developed. Some testing of a prototype scintillator has been performed; preliminary results will be presented here. In the meantime, data reconstruction times have been reduced, and the entire tomographic acquisition, reconstruction and volume rendering process streamlined to make efficient use of synchrotron beam time. A Fast Filtered Back Transform (FFBT) reconstruction program recently developed helped to reduce the time to reconstruct a volume of 150 x 150 x 250 pixels^3 (over 5 million voxels) from the raw camera data to 1.5 minutes on a dual R10,000 CPU. With these improvements, one can now obtain a "quick look" of a small tomographic volume (~l0^6 voxels) in just over 15 minutes from the start of data acquisition.

Keywords: X-Ray microtomography, synchrotron, real-time, parallel processing, porous materials

1. INTRODUCTION

X-Ray Computed Tomography provides nondestructive volumetric data of elemental composition, by mapping the three-dimensional X-Ray absorption through the sample. Consequently, tomography can be used to map spatial distribution and interconnectivity of pore or elements through a volume. X-Ray Computed Tomography was initially developed for clinical use in radiology in the 1970's. In the 1980's, the availability of synchrotron X-ray sources to the scientific community spawned a new generation of tomographic instruments. The high fluence of nearly collimated synchrotron sources made high spatial resolution X-ray transmission measurements possible. Similarly, the energy tunability of the broad synchrotron source spectrum allowed highly monochromatic and therefore element-specific measurements possible. Scientists from a variety of disciplines soon began to apply these source characteristics to the development and application of synchrotron X-Ray Computed Microtomography (XCMT) [1-6]. Commercial developments over the last decade in two-dimensional detector arrays, parallel architecture computing technology and 3-D visualization schemes have made XCMT even more attractive to researchers.

The third-generation XCMT instrument at the National Synchrotron Light Source (NSLS) Beamline X27A was not developed until 1995. The instrument is based on current 2-dimensional detector array and the latest processing technology. The goal since its inception has been the creation of a multidisciplinary tool for investigative research in a multitude of scientific disciplines[7]. Our goal was realized this past year with the formation of a Participating Research Team (PRT) that now funds and operates the X27A XCMT beamline. The PRT is a diverse group composed of nine members with applications ranging from biological to metallurgical. Microtomographic volumes of a broad range of samples have been produced this year at X27A including aerostructure materials, reservoir sandstones, rodent bones, insects, wood products, and

* Correspondence: E-mail: dowd@bnl.gov ; WWW: http://www.nsls.bnl.gov/ESG/beamlines/x27a/x27a.html ; PH: (516)344-7092

hydrated metal oxides. Resolutions vary with the size and type of sample, but the instrument is capable of resolving to less than two microns. Several applications are presented here to illustrate recent developments in the instrument.
Recent enhancements to the instrument have addressed the desire for real-time data acquisition and volume rendering and the need for highly monochromatic beam from below the Cr (6 keV) up to the Cs (36 keV) k-edge. A Fast Filtered Back Transform (FFBT) reconstruction program has been developed and implemented, that is based on a refinement of the "gridding" algorithm first developed for use with radio astronomical data.[8] This program has reduced the average reconstruction time to 8.5 sec for a 929 x 929 pixel^2 slice on a single R10,000 CPU, more than 8x reduction compared with the Filtered Back-Projection method using the same hardware. By applying these reconstruction and processing techniques, one can now obtain a "quick look" of a small tomographic volume (~l0^6 voxels) in just over 15 minutes from the start of data acquisition on our newly acquired dual R10,000 CPU Silicon Graphics Instruments (SGI) Octane/SE.

The monochromator design originally chosen for the XCMT beamline provided energy tunability from 5 to 13keV, with a $\Delta E/E$ of about 1.5%. When higher energies were necessary for other samples, the monochromator was lowered out of the X-Ray beam path, and the broad-energy or "white" beam filtered using metal foils to peak the energy spectrum as desired. This monochromator served its purpose but produced some problems. Though the desired effect of introducing a higher flux using these highly efficient multilayers was achieved, the low bandpass relative to the Si 111 at 10^{-3} to 10^{-4} $\Delta E/E$ for example, made k-edge subtraction studies difficult for most applications. In addition, more of our applications required a source energy above the 13 keV energy range provided by this monochromator. For these reasons we recently switched to a Si 111 channel-cut monochromator, providing highly monochromatic beam from just below the Cr edge to reasonably 36 keV or so. Extending our previous range of monochromatic beam and increasing the energy resolution from 1.5% to .1 % energy bandpass has improved image contrast for materials under study and will improve k-edge subtraction studies in the future.

The recent increase in monochromaticity, however, countermands our parallel efforts toward real-time data acquisition; higher monochromaticity yields a lower flux forcing longer data acquisition times. To balance the two, the pursuit of a more efficient scintillator for X-ray conversion to visible light has also begun. Presently, YAG:Ce has served well as the scintillator material. Its peak emission at 540 nm is better matched to the peak response of the CCD than most scintillating materials(see Figure 3). Also, its response time of .6 μsec is negligible relative to our exposure and acquisition times. Another important parameter is the stopping distance, or distance within the scintillator over which 1/e of the incident intensity is absorbed and subsequently converted. More efficient light collection and less noise from scatter will result from high stopping distances. If the goal were simply to collect as much light as possible, one would use a scintillator thick enough to absorb the X-Ray energy. When imaging, however, spatial resolution will be adversely affected if scattered light from a thick scintillator is collected. To maintain high resolution and increase the conversion efficiency, we are collaborating with Radiation Monitoring Devices on the design of a pixellated scintillator for X-Ray Microtomography. The goal of the design is to make use of the full stopping distance of the scintillator, while maintaining spatial resolution by minimizing scatter. Initial tests on a prototype scintillator design were recently performed with encouraging results. The scintillator fabrication process was validated and spatial resolution of the images was not limited by the scintillator. MTF curves performed by RMD on this pixellated scintillator show potential for superior image quality and high quantum efficiency in comparison to the YAG:Ce.

2. X-RAY COMPUTED MICROTOMOGRAPHY INSTRUMENT DESCRIPTION

2.1 Data Collection Instrument

The XCMT schematic and photograph are shown in Figure 1. X-ray CMT produces a cross-sectional map, or slice, of linear x-ray attenuation coefficients inside a small sample. In the X27A instrument, a 2-D detector array is used, so each slice will correspond to data collected in one row of pixels. To obtain the data for each reconstructed slice, the x-rays transmitted through a single slice of the sample are recorded on the row of pixels, which may be thought of as a linear array of detectors.

The sample is rotated, with the rotational axis perpendicular to the plane of incidence, by discrete angular intervals until it has traversed 180 degrees. The total number of views or X-Ray radiographs needed over the full 180 degree rotation is determined by the Nyquist limit for discrete sampling, and is $N\pi/2$, where N is the number of pixels per row. For each view, the transmission of each ray through the sample, along a line from the source to the detector is recorded at each pixel. This represents a line integral of the attenuation coefficients along this ray. The detector data for each view are then reconstructed using a novel Fast Filtered Back-Transform (FFBT) algorithm that implements a gridding technique for fitting to Cartesian coordinates.

The XCMT workstation at X27A, Figure 1, incorporates a cooled charge-coupled device (CCD) camera with 1317 x 1035 pixels, Kodak's KAF-1400 chip. Also available and regularly used for image recording is a 3072 x 2048 pixel chip, Kodak's KAF-6300 chip. Since the chip has 1035 rows of pixels, the CCD can record the data to reconstruct over 1000 horizontal slices, simultaneously. A thin high-resolution YAG:Ce scintillator with peak emission at 540nm is placed behind the sample to convert the x-ray attenuation map to a visible image. The image is magnified by a microscope objective and relayed by a 45 deg. mirror onto the cooled CCD area array. The use of imaging optics allows the flexibility to make a simple lens change and view larger samples with lower magnification, as desired. The mirror protects the camera and optics from direct X-Rays.[8]

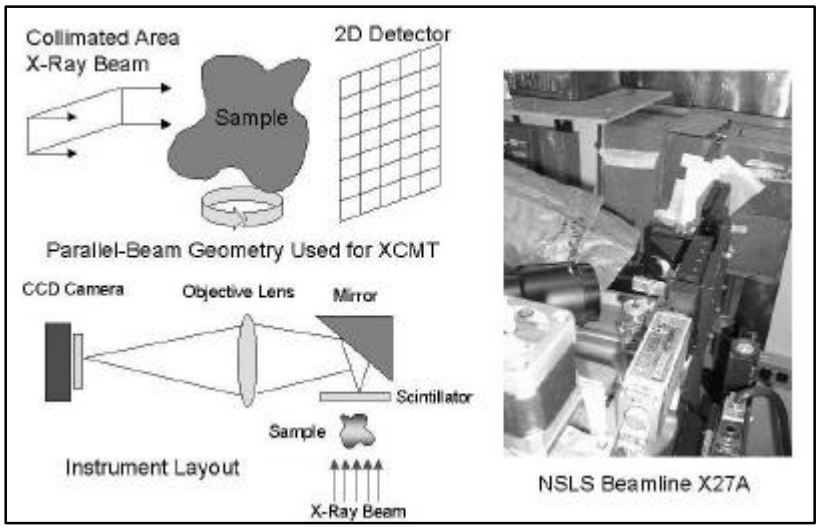

Figure 1. XCMT schematic and X27A photograph

With the current instrument, one can acquire data at a resolution of 2 microns over a field of view of about 3-mm in 1.5 hours. Larger fields of view of up to 27 mm (KAF-6300) can be obtained at proportionately lower resolution in the same amount of time. Long working-distance microscope objectives provide a choice of magnification of 1x, 3x, 5x, or 10x. A variable zoom microscopic lens of .75 to 3x magnification may also be used. Another variable is the pixel size. The KAF-1400 has 6.8-micron square pixels and the KAF-6300 has 9-micron square pixels. For a diffraction-limited lens, the pixel size, d, and optical magnification, M, will generally determine the resolution of the acquired data, d/M. Often, one is willing to sacrifice some resolution in favor of faster data acquisition and higher signal to noise ratios. When this is the case, the CCD may be binned so that NxN adjacent pixels are summed together and read out as one. This allows the user some control over the size of the sample that can be examined, data acquisition time, and resolution.

Of course, variability in the incident X-Ray energy spectrum is also crucial when different types of materials are to be studied on a day-to-day basis. Monochromatic beam is especially important for biological and environmental studies. The attenuation coefficient, μ, of an element is a function of both the energy of the X-Ray beam, and the atomic number, Z, of the element. The X-Ray Synchrotron emits a broad energy spectrum. X27A is at the bending magnet section of the ring, where the usable energy range is from about 5 to 50 keV. The attenuation coefficient of a material is strongly dependent on Z, the atomic number of the element, and on the incident X-Ray energy. As polychromatic X-Ray beam traverses a sample the shape of the energy spectrum changes, the lower end of the incident energy spectrum being absorbed more than the higher end. This property is called beam hardening.[9] Particularly for the lower Z elements found in environmental and biological samples, low energy and monochromatic beam of order 1% bandwidth or less are required to optimize contrast and minimize image artifacts from beam hardening effects.[10]

The monochromator design currently in place at the XCMT beamline uses a channel-cut Si 111 crystal. Energy tunability is from < 6 keV to 36 keV, with a $\Delta E/E$ of 10^{-4} to 10^{-3}. If higher energies are necessary and photon flux becomes an issue, the monochromator can be lowered out of the X-Ray beam path, and the broad-energy or "white" beam filtered using metal foils to peak the energy spectrum as desired.

3. INSTRUMENT ENHANCEMENTS

3.1. Monochromator

Until recently, the monochromator in place at the XCMT beamline incorporated a highly efficient pair of W-B_4C multilayers deposited on Silicon substrates made by Osmic, Inc. Energy tunability from 5 to 13keV, with a bandpass of about 1.5% is possible with this monochromator. This design was chosen to obtain a high photon flux at the lower energies used for

biological and environmental applications, where beam hardening effects are especially noticeable. Its properties are well matched to the synchrotron source beam.[11]

For the geological and metallurgical applications, however, energies above 13 keV are required. In addition, for k-edge subtraction tomography, a higher energy resolution was needed. The multilayer monochromator was subsequently replaced with a Si-111 channel cut monochromator with tunability from below 6 keV up to at least 36 keV and narrow bandpass of 10^{-4} to 10^{-3} depending on the collimation and height of the X-ray beam on the crystal.. Figure 2 shows a scan of energy resolution for a similar Si 111 channel-cut mono located at the X18B beamline at NSLS. In anticipation of the increased exposure times needed with this highly monochromatic energy profile, we began a search for a more efficient scintillator last year, to replace the current YAG:Ce crystal.

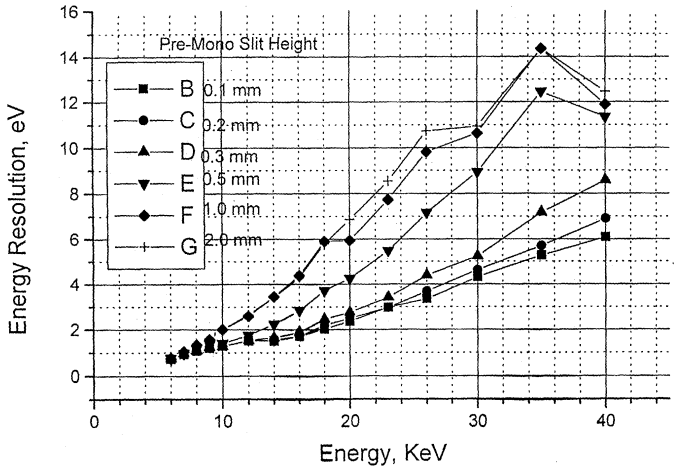

Figure 2. Energy resolution of the Si(111) channel-cut monochromator at X-18B. Energy resolution measured here is the FWHM of the monochromator rocking curves as a function of energy. Height of beam on crystal was 1 mm.
Figure provided by Syed Khalid, X18B Local Contact (khalid@bnl.gov)

3.2. Scintillator

Presently, YAG:Ce has served well as the scintillator material. Its peak emission at 540 nm is better matched to the peak response of the CCD than most scintillating materials (Figure 3). At 540 nm, the CCD is at 80% of its peak response which is around 700 nm. A disadvantage of YAG is its overall low energy conversion. Another important parameter is the stopping distance, or distance within the scintillator over which 1/e of the incident intensity is absorbed and subsequently converted. More efficient light collection and less noise from scatter will result from high stopping distances. The stopping distance is related to high density. As one can see from Table I below, YAG is inferior to some of the scintillators commonly used, such as cadmium tungstate, but superior to many others in its stopping power. The high magnification lenses typically used have 1 to 10 micron depths of focus. To bring all of the light collected to a good focus, therefore, a scintillator crystal with extremely high stopping power (short stopping distance or attenuation length) would be needed, in addition to fast decay times and high-energy conversion. A discussion of factors that drive the design of a structured scintillator and the status of this work is given here.

The quality of the tomographic slices generated using the present lens-coupled system is determined largely by image resolution and contrast of the X-Ray radiographs, but also by noise in the reconstruction algorithm. In the best case, one would be able to reconstruct to the resolution of the acquired CCD images, which in turn, would be limited by the imaging optics. Assuming good quality, diffraction-limited optics are used to image the transmission map at the scintillator, the smallest resolvable feature at the scintillator is $r = .61\lambda / NA$, where NA is the Numerical Aperture of the lens, and λ is the wavelength of the scintillator emission. This is derived by assuming that two point sources can be resolved as being separate when the center of the Airy disc from one overlaps the first dark ring in the diffraction pattern of the second; this is known as the Rayleigh criterion.[12]

At the image plane, this resolvable spot is magnified by the power of the optics, and will be $d_i = M (.61 \lambda/NA)$ where M is the magnification. The CCD at the image plane samples the magnified transmission map, by discrete lengths determined by the pixel size. To properly sample the data without loss of resolution, according to the Nyquist limit, you must sample at least twice within each length to be resolved; in other words, d_i must span across at least 2 pixels to be resolved by the camera.

$$d_i \geq 2l, \quad \text{where l is the length of a pixel}$$

or $$M (.61 \lambda/NA) \geq 2l .$$

Increasing M beyond the equality condition only serves to reduce S/N and reduce the field of view; matching the above condition is best. For the Nikon 10x lens that we often use, the NA is .2. The peak emission of the YAG:Ce scintillator is about 540 nm. The resolvable distance is then about 1.7 microns, or 17 microns at the CCD detector. This is matched reasonably well with both the KAF-1400 (6.8 microns/pixel) and the KAF-6300 (9 microns), allowing the potential for

diffraction-limited image resolution. There are, however, other issues, which must be considered in optimizing the instrument for optimal resolution of these acquired images. The instrument must be optimized to take into account physical properties of the specimen to be measured, the characteristics of the x-ray beam available to probe the specimen, signal to noise (S/N) ratios needed in the reconstructed image, and requirements of the data processing algorithm[13]. In particular, the desired S/N ratios impose stringent performance requirements on individual detector components. Thus, the x-ray detectors with higher detective quantum efficiency (DQE(f)), which is defined as the square of the ratio of the output $(S/N)_o$ to the input $(S/N)_i$, are preferred. Higher DQE(f) performance requires detectors with higher spatial resolution while maintaining high x-ray detection efficiency and low noise. This is particularly important for real-time and in vivo measurements as an order of magnitude increase in voxel resolution requires three orders of magnitude increase in exposure, making the latter impractical due to excessive radiation doses.

In micron-resolution applications, the scintillator often sets the limiting resolution, because of scattering of the scintillation photons. There are conflicting requirements of ensuring high x-ray absorption (i.e., thick scintillator) to collect all the light generated through the sample (depends on the stopping distance of the material) and low optical scattering (i.e., thin scintillator) [14]. Since the depth of focus of a fast objective lens is limited (<1 μm for 100x lens, 14 μm for a 10x), the useful signal is only collected from a thin front layer; light generated through the rest contributes only to noise. Thin scintillators are ideal for maintaining spatial resolution therefore, but thicker screens (50 μm or greater), are required to provide reasonable detection efficiency for x-ray energies typically used in microtomography (8 to 40 keV). Thus, the development of a sensor that allows increased thickness without sacrificing spatial resolution would dramatically improve the performance of the existing XCMT scanners.

RMD Inc. is currently developing a novel scintillator, which overcomes these limitations. The new design consists of a finely pixelized array of CsI(Na). Each of the pixels will function as an optical waveguide. Thus, the scintillation light produced in each pixel is preferentially channeled towards the optical detector preventing the lateral light spread and enhancing the spatial resolution. The process allows fabrication of very thick pixel structures with increased x-ray absorption, overcoming the traditional tradeoff between detection efficiency and resolution resulting in a high DQE(f). Table I summarizes properties of various scintillators currently used for XCMT application. [15]

Table I: Properties of various scintillator screens currently used for XCMT[15]

Scintillator	Type	Light Output (Photons/MeV)	Density (g/cc)	Decay Time (ns)
YAG:Ce	Crystalline	11,000	4.55	290
CdWO4	Crystalline	28,000	6.1	6000
BGO	Crystalline	8200	7.13	300
ZnS:Ag	Powder	49,000	4.09	200
Gd2O2S:Tb	Powder	30,000	3.01	>0.5 ms
CsI(Na)	Crystalline	42,000	4.51	630

A wide variety of materials may be used, but CsI(Na) was chosen for initial testing based on its properties[16,17]. First, CsI(Na) has a high stopping power (density = 4.5 g/cm^3, average atomic number = 51), second, it exhibits very high scintillation efficiency (410 photons/10 keV), and finally, a fast scintillation decay time of 630 ns which is necessary for rapid data collection. A disadvantage of using this material is that the 430 nm peak emission of CsI(Na) is not well matched to the spectral response curve for the front-illuminated Kodak KAF-1400 & 6300 chips used at X27A (Figure 3). Nevertheless, the high specific stopping power and excellent light transmission characteristics of CsI(Na) should decrease the quantum dependent noise contributions[18]. On a practical level, CsI(Na) is widely available and can be readily vapor deposited to form large area screens.

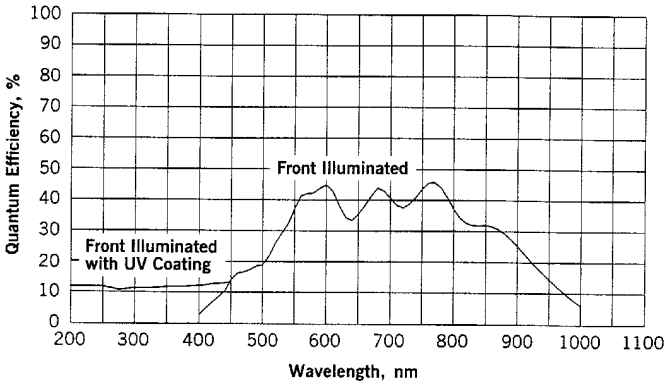

Figure 3. Spectral-response curve for the front-illuminated KAF-6300 chip in Princeton Instruments Model CCD-3072-K. (from Princeton Instruments "Catalog of High Performance Digital CCD Cameras", October 1994.)

3.2.1 Scintillator Measurements. A quantitative characterization of the new CsI(Na) imaging sensor has been performed to compare its performance to that of a YAG:Ce crystal. These studies were performed using a CCD detector with a front-illuminated 1024 x 1024 Tektronix CCD with a fiberoptic window. The CCD pixel size is 27 μm, resulting in an intrinsic Nyquist limiting resolution of 18.5 lp/mm. The CCD was thermoelectrically cooled to -20°C to minimize the noise. The scintillator screens were coupled to the fiberoptic CCD window using an index-matching oil. The CCD integration time was varied between 1 to 5 seconds depending on the light emission efficiency of the screen under evaluation and the type of measurement being made. The 16 bit CCD image data were transferred to a PC for image processing and analysis. The beam incident on the detector was generated by a tungsten target X-ray generator set at 30 keV. The detector was positioned approximately 45 cm from the X-ray source in order to illuminate the scintillators uniformly.

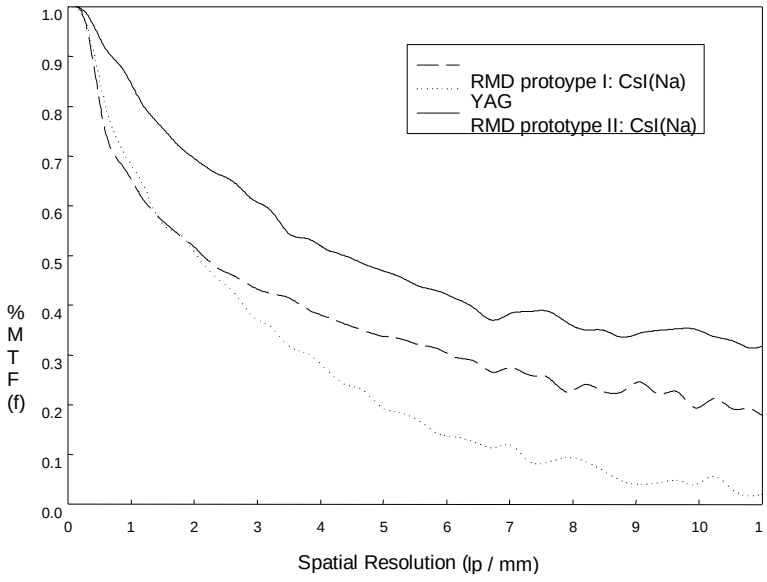

Figure 4. Spatial resolution (MTF(f)) of a prototype RMD pixelated CsI(Na) and currently used YAG:Ce crystal.

3.2.1.1 Light output measurements.
The 100 μm thick CsI(Na) samples exhibited approximately a factor of 3 higher light output per x-ray relative to the 250 μm thick YAG screen. This is primarily due to the high light conversion efficiency of CsI(Na) (42,000 photons/Mev)[15] and excellent light transmission properties of the crystalline pixels.

3.2.1.2 Spatial resolution measurements. The modulation transfer function, MTF(f) for spatial frequencies in the range of 0 to 11 lp/mm for various crystalline scintillators was calculated from the Fourier transform of the line spread function (LSF) data. The CCD detector was the same Tektronix fiberoptic-coupled CCD described above. A 10-μm wide tantalum slit was placed in front of the scintillator under test at a 0.97°angle with respect to the CCD pixel columns. This resulted in a highly sampled LSF sampling frequency of 0.45 μm, which eliminated the aliasing artifacts in the MTF calculation. Figure 4 compares the MTF(f) for two prototype CsI(Na) designs and YAG:Ce converter. The prototype CsI(Na) screens displayed significantly higher spatial resolution compared to the YAG:Ce crystal. For this detector configuration, at 10 lp/mm the prototype I pixelated CsI(Na) screens exhibited a factor of five improvement in MTF compared to the YAG:Ce scintillator.

3.2.1.3. Microtomography measurements at X27A. To assess the imaging performance of the new scintillator, a 100 μm thick CsI(Na) screen from RMD was incorporated into the XCMT instrument at the X27A beamline. Tomographic slices through a trabecular bone region of the tibia of a normal adult laboratory rat, part of a study on osteoporosis, were generated. The 6.8-micron square KAF-1400 CCD pixels were binned by a factor of 2x in both directions resulting in a digital pixel resolution of 13.6 microns. A reconstructed slice of the data through the middle of the reconstructed volume is shown in Figure 5.

For comparison, the same data set was measured using the YAG:Ce single crystal scintillator (Figure 5). While the CsI(Na) sample showed expected high resolution (13.6 μm, limited by the CCD pixel size used) the image contrast was not as high as expected. The primary reason for the reduced contrast was most likely the presence of a few small high intensity spots in the RMD sample. To prevent these areas from saturating, the exposure time had to be reduced, subsequently reducing the overall dynamic range and intensity contrast of the acquired images. Improved care in the preparation of the screens is expected to eliminate this problem. Based on these MTF curves and XCMT scans, the next-generation scintillator screens are expected to dramatically improve the performance of X-Ray Computed Microtomography instruments.

3.3. Data Reconstruction

The raw data files are saved as they are collected to either a local or remote drive, for subsequent processing. Because each slice is computed independently, reconstruction is trivially parallelized by parsing the reconstruction of slices to parallel

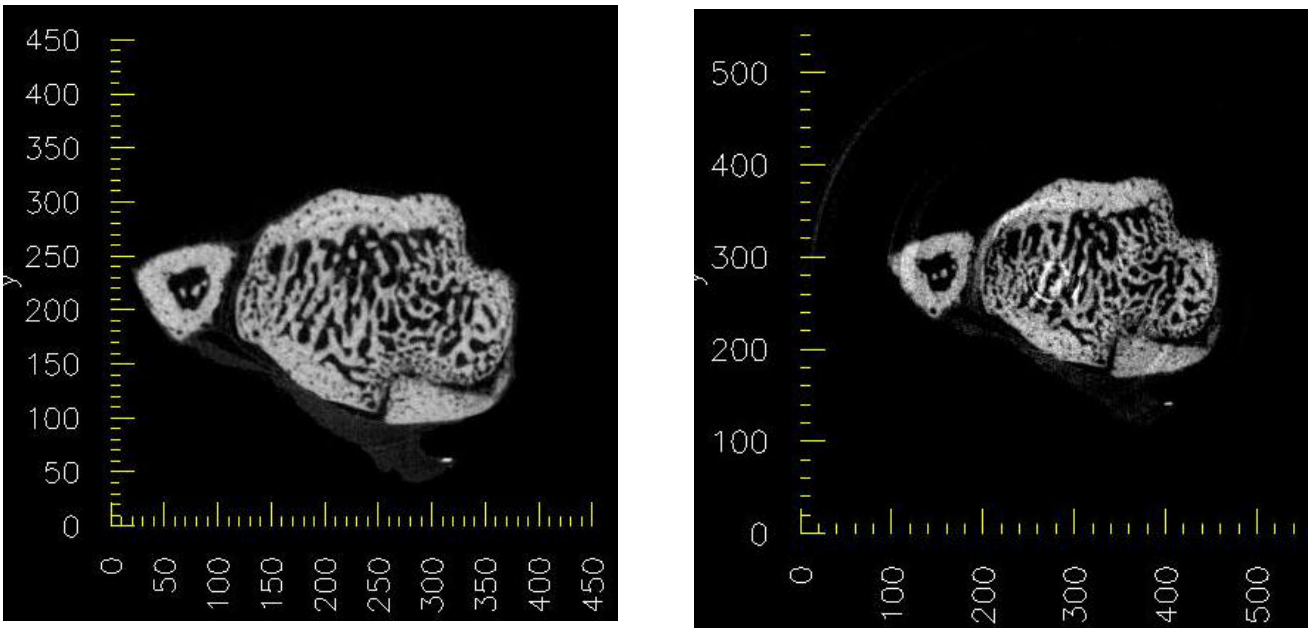

(a) (b)

Figure 5. Tomographic slices through a trabecular bone region of the tibia of a normal adult laboratory rat generated using (a) the YAG:Ce and (b)RMD prototype CsI scintillator.

processors. No additional software for parallel processing is required, as it is for Parallel Virtual Memory (PVM), for example. Computational time for the reconstruction of a 656 x 656 x 656 pixel^3 volume or 280 million voxels currently stands at 30 minutes, using an on-site Pentium farm running eight Symmetric Multiprocessors (SMP). The Fast Filtered Back Transform (FFBT) used for the reconstruction is described in the section that follows.

3.3.1 Fast Filtered Back Transform for Microtomography

The mathematics of the various reconstruction methods for tomography have been well-documented[19-20, 9] and are discussed here. The attenuation through a homogeneous material is represented simply by Beer's law:

$$I_t(x') = I_0(x') [\exp(-\mu L)] ,$$

where μ is the linear attenuation coefficient for the material in inverse length units, L is the length of material traversed by the transmitted beam, and x' is the point along a perpendicular to L at which the transmitted beam is detected. $I_t(x')$ and $I_0(x')$ are the transmitted and incident intensity respectively at x'. For a nonuniform slab of material where μ is a function of the material coordinates (x,y),

$$I_t(x') = I_0(x') \exp[-\int_L \mu(x,y)\, dy']$$

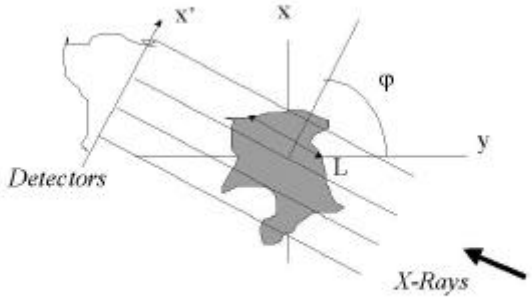

Figure 6. Projection Data

This is a description of the signal recorded at each detector for each view. The entire set of data collected in a slice can then be described as the set of $I_t(\varphi, x')$ where φ represents the view angle. From the recorded data I_t and I_0 , one can describe a single view or projection of the sample as

$$P(\varphi, x') = -\ln [I_t(\varphi, x') / I_0(\varphi, x')]$$

$$= \int_{\infty}\int_{\infty} \mu(x,y)\, \delta(x \cos\varphi + y \sin\varphi - x')\, dx\, dy$$

where $\delta(x \cos\varphi + y \sin\varphi - x')$ is the Dirac delta function and defines the path, L, through the sample of the line integral. The reconstruction then becomes an inversion problem to recover $\mu(x,y)$ from the recorded view data. Reconstruction techniques fall into the three general categories of iterative techniques, filtered backprojection (FBP) and Fourier Transform (FT) methods. The Fast Filtered Back Transform (FFBT) developed and applied to the NSLS XCMT projection data falls into the last category. These Fourier Transform (FT) methods are based on the Central Slice Theorem, also known as Fourier Slice Theorem, which relates the 1-dimensional FT of a projection, $P(\varphi, x')$, to the 2-dimensional FT of the density function, $\mu(x,y)$, that describes the sample. By plotting the 1-D FT's from the many views on a polar grid, one can fill up the frequency domain as a function of the polar coordinates of the sampled data.[21] The potential advantage of FT methods lies in the possibility of using the Fast Fourier Transform (FFT) to perform the inverse 2-D FT in a number of steps on the order of $N^2 \log N^2$ for an N x N pixel array, compared with on the order of N^3 steps for the filtered backprojection (FBP) method. This requires, however, that the polar grid data be somehow mapped onto a Cartesian grid in a comparable or smaller number of steps. The traditional approach is to use some relatively simple local interpolation scheme to carry out the polar-to-Cartesian mapping. Despite considerable difficulties encountered in early attempts, several successful Fourier reconstruction algorithms using interpolation were developed in the 1980's [6,19]. Generally speaking, they require oversampling the FT to some degree in the radial direction, for which the interpolation error can be shown to be most critical.[19]

With the FFBT algorithm, a somewhat different technique called "gridding" is employed. Gridding was first developed by radio astronomers for use in aperture synthesis as a means to back-transform irregularly sampled Fourier data. Since then it has been suggested as a robust method of reconstruction for computed tomography[22] and implemented for MRI data.[23] Succinctly put, the data on the polar grid are first weighted (or 'filtered') by factors which take into account the non-uniform area elements on the polar grid. The weighted data set is then mapped onto a Cartesian grid -- not by simple interpolation, but by convolution with the Fourier transform of a certain function, *w(x,y)*. Next, the 2-D inverse FFT is applied, and finally, the resulting image is divided by *w(x,y)* to correct for the effects of the convolution.

The function *w(x,y)* can be chosen so that its Fourier transform vanishes for spatial frequency magnitudes larger than a few grid spacings, while *w(x,y)* itself remains well concentrated in the region of interest. Then the number of steps needed for the convolution scales only as N^2, while aliasing artifacts arising from the discrete Cartesian sampling remain small. In our implementation, we use for *w(x,y)* a separable form, *w(x)w(y)*, with *w(x)* chosen from the family of (1-dimensional) Prolate Spheroidal Wave Functions (PSWFs) of zeroth order[24]. Every such *w(x,y)* has the property that it is *maximally* concentrated in a square region of interest, subject to the constraint that its Fourier transform vanishes outside a given square centered on the origin in frequency space. Tables of the desired PSWF and its Fourier transform can be efficiently computed and stored at run time, using known rapidly converging expansions of PSWFs in terms of Legendre polynomials[25].

The FFBT has essentially the same speed advantages as the Fourier methods based on interpolation, with some additional benefits. The user can specify the desired origin, size and resolution of the region to be displayed. Choosing a smaller region and/or a lower resolution decreases the number of grid points needed in the 2-D FFT. In this way, extremely fast "quick-look" reconstructions become possible, even with large data sets. The FFBT also has potential application to other problems in tomography that can be described as having irregularly sampled points, such as the limited angle problem.[22]

3.4. Integration of Data Acquisition, Reconstruction and Rendering: Streamlining

The development of the FFBT and enhancement of the raw data processing software have significantly reduced the reconstruction time and improved the user-friendliness of the XCMT instrument. Improvements in both hardware and software centering have basically eliminated the need to "tweak" the centering of sinograms in the software as was done in the past. The software centering routine locates the center of rotation by finding the center of gravity of each of the slice sinograms. Because the initial experimental alignment is so precise, we only need then to compute the average center value over all slices and use that value for the reconstruction of every slice.

Now at the completion of data acquisition, a script is automatically generated and at the user's discretion, can be run automatically upon completion of the data acquisition. The automated output is a full reconstruction and volume rendering from the reconstructed data, with no additional user intervention required. Figure 9 shows a subvolume of tomographic data that was acquired, fully reconstructed and rendered in 16 and a half minutes: 15 minutes for data acquisition and one and a half minutes for reconstruction and rendering. Shown is a 50-pixel-cubed subvolume of this hydrated iron oxide sample. Each voxel measures 1.4 microns-cubed. To generate the volume, 250 views of 12-bit camera images of size 158 columns x 254 rows were collected. Exposure time was 1.2 seconds. The Si 111 monochromator was used with the energy tuned to 8.5 keV. The figure was quickly composed using Fortner Software's T3D software.

4. TOWARD REAL-TIME XCMT

4.1. XCMT Hardware benchmarks.

The reconstruction process has been divided into three phases. Phase I creates the sinograms from the normalized raw camera data. Phase II applies noise and artifact reduction filters and Phase III performs the Fast Filtered Back Projection (FFBT). We call the latter "Gridrec" in reference to the gridding algorithm on which it is based. The data acquisition and reconstruction steps will have to be better integrated in order to achieve our goal of "real-time" XCMT. The streamlining described above is a first step toward this integration. Eventually, we will need to begin processing as the data is acquired. Presently, the view data is normalized or flat-fielded before being saved to disk. The next step will be to generate the sinograms as each view is acquired and write to the open sinograms as well as save the raw camera data. The generation of the sinograms and subsequent filtering consume more time than the actual reconstruction in Phase III. Phase I is particularly troublesome since it is not parallelized; running more processes on more CPU's won't help. But with the proper hardware, we are hoping eventually to perform Phase I synchronously with data acquisition, which presently takes more time than all the software processing combined.

The specification of a parallelized Symmetric Multiprocessor (SMP) cluster dedicated to XCMT for fast data acquisition, reconstruction and rendering is underway for the next major instrument upgrade The addition of additional CPU's will speed-up Phase II and III which are applied to each slice data, and so are trivially paralellized. The following table summarizes the results of running our present codes on a dual processor 500 MHz Pentium III running Linux , available to us for benchmarking and on the SGI Octane SE dual R10000 presently used for reconstruction and volume rendering. The test volume consisted of 720 views, each view being 458 x 128. (i.e. 128 slices). The results for Phase II and Phase III are the average of the two times. All entries are in seconds. The CPU time is that time the process is actually executing, the SYS time is the processor time spent executing system functions on behalf of the process. Real entries are the elapsed wall clock time. Note that these numbers are the result of a single run.

The Gridrec step in the calculation is heavily floating point and demonstrates the relative weakness of the Pentium for floating point calculations. The "Total Real" numbers are greater than the sum of the individual real time numbers because the calculation was done in two parallel streams, using the two processors on each system. For each step, the reported number is the average of the two streams, however for the total, the number measures from beginning to end (and is approximately the sum of the maximum of the two streams).

Table II. Processing Benchmarks

	PhaseI CPU	Phase I SYS	Phase I Real	Phase II CPU	Phase II SYS	Phase II Real	Gridrec CPU	Gridrec SYS	Gridrec Real	Total Real
Pentium III	6.13	3.04	16.84	9.83	4.34	33.80	67.19	3.37	83.25	152
SGI Octane	4.475	2.783	37.54	8.276	3.435	32.48	48.315	1.652	62.25	136

There are two reasons that performance will not scale directly with the number of processors available. One is that the Phase I step is not parallelizable and will stay constant. The other is the problem of distributing the data to the processors doing the calculation. Since each file involved is only read and written once, the normal approach is to read the files using NFS from where they originally reside. However the Linux implementation of NFS is relatively poor and it might prove faster to copy the data from disk to disk and then access it locally. The additional overhead from each of these approaches has not yet been evaluated. If we estimate the speedup possible by using 10 processors, the 118 sec of Phase II and Gridrec could be reduced to 12 sec. If we allow 4 sec for data moving, then the 152 sec could be reduced to 33 sec for a speedup of 4.6. At this point, it will become necessary to consider ways to speed up Phase I.

5. SOME APPLICATIONS

5.1. Biomedical. The volume processed for the hardware benchmark studies was a 458 x 458 x 128 pixel-cubed region of the trabecular bone of the tibia of a normal adult laboratory rat, approximately 2.5 mm from the joint cartilage. A Nikon 1x achromatic objective was used to image the shadow on the YAG:Ce onto the CCD. The KAF-1400 6.8 micron pixels were electronically binned by a factor of 2x in x and y resulting in a digital pixel resolution of 13.6 microns-squared. A 100 x 100 x 75 voxel cube of the data is shown in Figure 8. XCMT volume data of trabecular bone such as the one depicted here is being used in ongoing studies in bone morphology and osteoporosis in collaboration with the Program in Biomedical Engineering at SUNY, Stony Brook. The increase in quantum efficiency expected with the proposed scintillator design and other instrument improvements will hopefully make in vivo bone studies possible in the future.

5.2 Hydrous iron oxides. To understand and model contaminant bioavailability and mobility, contaminant distribution processes must be understood. Although the subsurface system is comprised of a number of sorbents, amorphous oxides are an important phase in controlling metal contaminant distribution because they exist not only as discrete particles, but also as coatings on other minerals. Sorption reactions between the bulk aqueous phase and organic matter and/or clay are readily reversible, as a result adsorbates are eventually redistributed to porous, amorphous oxides where in the slow sorption process of surface diffusion, the particle acts as a sink for the contaminant. Likewise, when the contaminant desorbs, a constant source of contaminant exists, which is presently not included in hydrogeochemical transport models and not accounted for during site remediation.

Because amorphous iron and manganese oxides have large surface areas, microporous structures, and very high affinities for metal contaminants, they are one of the most important surfaces for contaminant binding. Although amorphous iron and manganese oxides are metastable, the presence of contaminants has been observed to inhibit their crystallization. Many traditional characterization methods, like those for surface area, involve assessing freeze-dried particles, which are most likely quite different from the hydrated form found in the environment.

A volume of hydrous iron oxide is shown in Figure 9. The volume shown was acquired with a 5.4-micron pixel resolution, and with the Si 111 tuned to 8.5 keV. This is the same volume used as an example for automated data acquisition and reconstruction. Higher resolution scans on the order of 2 microns have been acquired as well. These studies are on-going. Future work will apply K-edge subtraction tomography to enhance image contrast using the newly acquired Si 111 monochromator.

5.3. Geological Studies for Oil Recovery Systems

Certain heavy, viscous crude oils demonstrate unusual flow characteristics that result in robust recovery that is higher than expected. These crudes typically contain a small concentration of dissolved gas (generally methane, at 10-20 scc/cc oil) that help displace the oil from the formation as the pressure declines and the gas is depleted from the oil. It is widely speculated within the oil industry that the nature of the nucleation and the resulting transport of the gas bubbles may be responsible for the flow characteristics. Although this drive mechanism is generally present in conventional low viscosity oils (known as “solution gas drive”) the robustness is generally enhanced in viscous oils. Many have theorized that “microbubbles” are formed, and that the viscosity of the solution inhibits the coalescence of the nucleated bubbles. Although there have been micromodel studies (etched 2-D visual models that attempt to mimic real porous media) of the viscous oil depletion with resolutions down to 2 microns, there have been no direct observation of the bubble formation and transport in a porous media.

A very simple set of experiments was designed in an attempt to image the bubbles during pressure depletion. Conventional 1/4” aluminum tubing was filled with sand recovered from the reservoir of interest. The pore space of the tube was then

filled with water representative of the formation, and then displaced with "live" heavy oil (oil with dissolved gas). In this manner, the sandpack contains a representative combination of oil and water from the formation. The bubble point (saturation pressure) of the oil was approximately 1100 psi, and the oil initially contained approximately 18 scc of gas/ cc oil. The pressurized tubes were shipped to the NSLS, and were connected to flexible nylon tubing (to allow the tube to be rotated during the imaging) and then pressurized with nitrogen. The upper part of the tube was wrapped with heating tape, insulated, and maintained at the formation temperature (129 F). The portion of the tube to be imaged was left bare. The tube was imaged at the initial pressure (~1500 psi) and then imaged at other pressures as the tube was depleted. In one case, the tube was depleted in 200 psi increments, and in the other case, the tube was depleted in 100 psi increments.

The entire tube was imaged at a source energy centered around 20 keV, using metal foils to peak the X-Ray source. Both 1x1 (1013x1013, 6.8 micron resolution) and 2x2 binning (505x505, 13.6 micron resolution) were utilized for imaging. Figure 10 shows two reconstructed slices at 1500 psi (no pressure reduction). There should be no bubbles present, though a few very small regions that may be bubble were observed. There is clear evidence of bubbles at the low pressures (< 300 psi); however, it is imperative for a successful study to be able to identify the bubbles in the region just below the saturation pressure (ie, 700-1100 psi). Work continues on the image processing. In the next set of experiments, several improvements are proposed to improve the sample preparation procedure and to minimize movement of the sample during depletion and rotation. Furthermore, a 1/8" tube may be utilized to allow resolutions down to 3.4 microns. Additionally, the recent implementation of the Si 111 monochromator should yield a better separation of the attenuating elements, resulting in improved identification of the gas regions. Plans for faster data acquisition will also ensure that there is no image blur during acquisition due to movement of the bubbles.

5.4. Aerostructure Materials

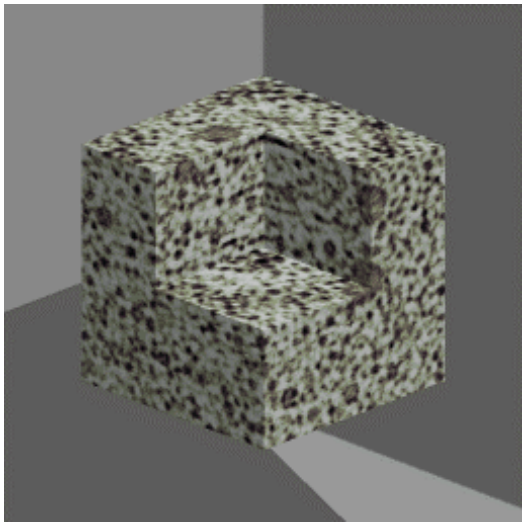

A few different groups have been examining various types of aerostructure materials with XCMT. A volume rendering of one such material, a porous polymer, is shown in Figure 7. Polymers have many applications including packaging, shock absorption and noise abatement. Present studies are focussed on material microstructural characterization and microstructure-scale deformation. Compression and other tests have been performed in the past using microscopes to observe structural changes.[26] Often, mechanical sectioning was necessary. This sample preparation could result in damage to the sample under test. The use of XCMT avoids these types of problems. In-situ compression tests are underway that allow the impact of external compression through the entire volume to be analyzed using XCMT.

Figure 7. 100 pixel-cubed ($1.4mm^3$) volume with a cutout, of a porous (51%) polymer acquired using the Si 111 monochromator tuned to 14 keV. Voxel size is 13.6 microns-cubed. The avg. D of the Expancel (small spheres) is 30-50 microns. Sample and data from R. Everett & K.Simmonds, NRL, Washington. D.C.

6. ACKNOWLEDGEMENTS

This work was supported by the U.S. Dept. of Energy under grant No. DEA-C02-76CH00016, Office of Energy Research.

The author wishes to give special thanks to the following for their contributions to this paper: Tim Ellison of Mobil E&P Technical Center in Dallas for contributions to Section 5.3 (tim_k_ellison@email.mobil.com) and Rick Everett and Kirth Simmonds of the Naval Research Laboratory in Washington, D.C. for their timely contribution to Section 5.4 (everett@anvil.nrl.navy.mil; simmonds@anvil.nrl.navy.mil). I also thank Syed Khalid from NSLS for providing the plot of Si-111 energy resolution.

Finally, a special thanks to all the **PRT members** for their continuing support of the NSLS XCMT beamline and for helping to make this first year a success. In addition to the NSLS, the PRT member organizations are: SUNY, Stony Brook, Dpt. Of Material Science; National Taiwan University, Dpt. Of Geology; Naval Research Laboratory; Dpt. Of Applied Science at BNL;Northrop-Grumman Corporation; Mobil Corporation: Lousiana State University, Dpt. Of Geology; and Forest Products Laboratory/Univ. of Wisconsin, Madison.

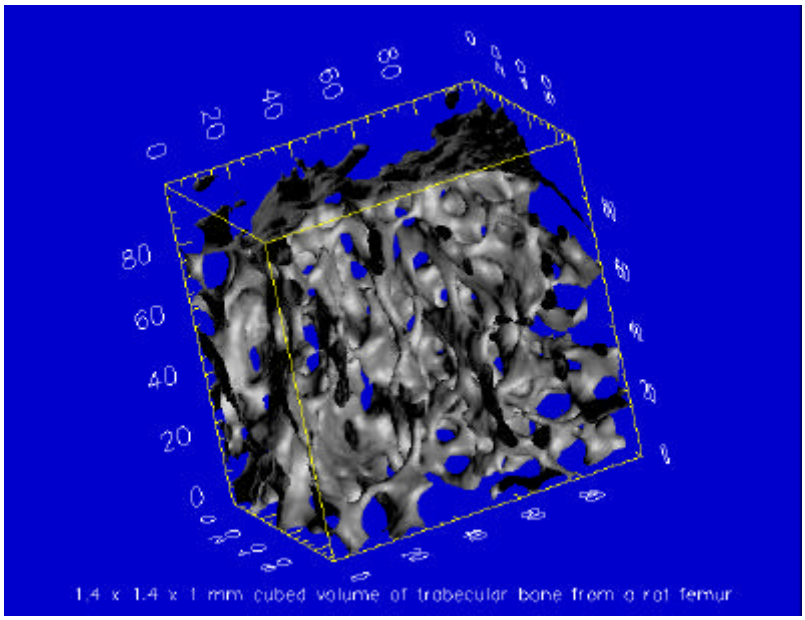

Figure 8. Trabecular bone volume from the tibia of a normal laboratory rat taken at 13.6 micron-cubed digital resolution. Bone sample provided by Mitchell Belzer, United Research Corp., Rockville, MD.

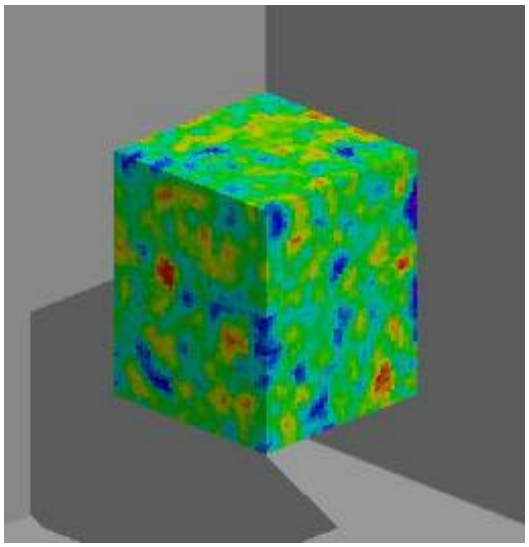

Figure 9. A 68 x 68 x 68 micron-cubed volume of hydrous iron oxide. The densest material, iron oxide appears green and red and the lightest, water, appear blue. Dark blue areas are purely liquid phase, while light blue areas are most likely highly hydrated iron oxide surfaces.

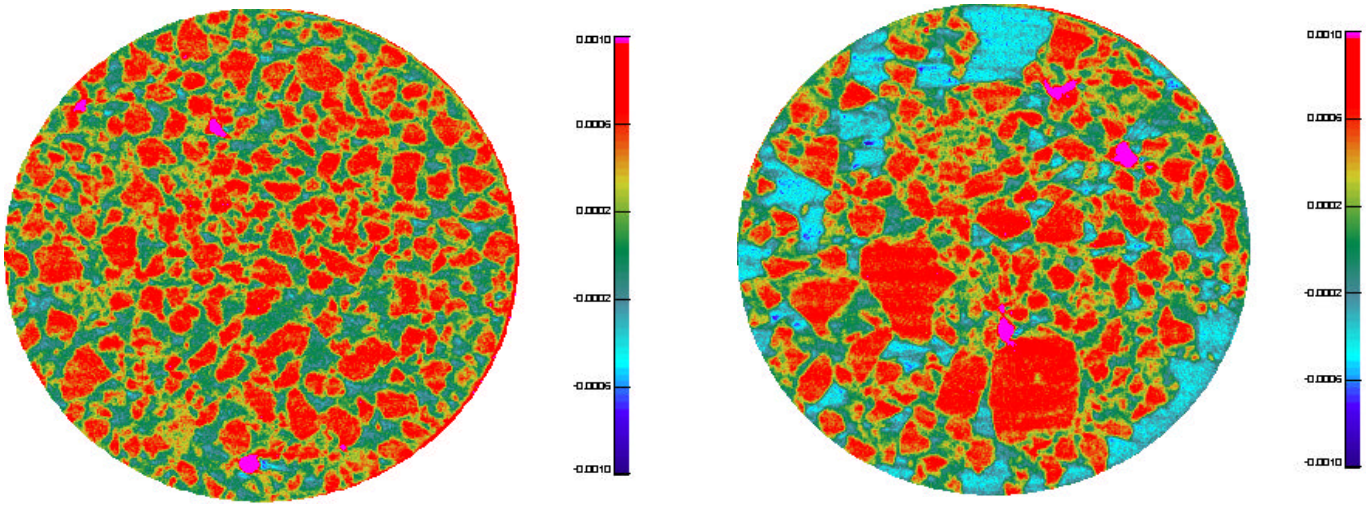

Figure 10. A reconstructed slice of the sample at 1500 psi (left), and at the fully depleted 14.7 psi (right). Gas bubbles are colored bright blue. A few small regions that may be gas are seen in the left figure. Quite large nucleated bubbles are present as expected in the slice from the depleted sample. Solid is colored red and oil/water mix is green. Data & Figure provided by Tim Ellison, Mobil E&P Research Corporation, Dallas, TX.

7. REFERENCES

1. L. Grodzins, "Optimum Energies for X-Ray Transmission Tomography of Small Samples: Application of Synchrotron Radiation to Tomography", *Nucl. Instrum. and Meth.*, **206** (1983) 541.
2. K.L. D'Amico, H.W. Deckman, J.H. Dunsmuir, B.P. Flannery, W.G. Roberge, "X-Ray Microtomography with Monochromatic Synchrotron Radiation", *Rev. Sci. Instrum.*, **60:7** (July 1989) 1524-1526.
3. P. Spanne, M. Rivers, "Computerized Microtomography using Synchrotron Radiation from the NSLS", *Nucl. Instrum. and Meth.*, **B24/25** (1987) 1063-1067.
4. U. Bonse, Q.C. Johnson, M.C. Nichols, R. Nuflhardt, S. Krasnicki, J. Kinney, "High Resolution Tomography with Chemical Specificity", *Nucl. Instrum. and Meth.* **A246** (1986) 644-648.
5. J. Kinney, Q.C. Johnson, M.C. Nichols, U. Bonse, R. Nuflhardt, "Elemental and Chemical-State Imaging Using Synchrotron Radiation", *Appl. Optics*, **25** (1986) 4583-4585.
6. B.P. Flannery, H.W. Deckman, W. Roberge, K.L. D'Amico, "Three-Dimensional X-Ray Microtomography", *Science*, **237** (Sept. 1987) 1439-1444.
7. B.A. Dowd, "Synchrotron X-Ray Computed Tomography at the NSLS", *NSLS Newsletter*, (July 1996).
8. B.A. Dowd, A.B.Andrews, R.B. Marr, D.P.Siddons, K.W. Jones, A.M. Peskin, "Advances In X-Ray Computed Microtomography at the NSLS", *Advances in X-ray Analysis*, Vol**. 42**, May 1999.
9. G.T. Herman, *Image Reconstruction From Projections*, Academic Press (1980).
10. F.A. Dilmanian, "Computed Tomography with Monochromatic X-Rays", *Amer. Jour. of Physiol. Imag.*, **3/4** (1992) 175-193.
11. M. Hart, L.Berman, "X-Ray Optics For Synchrotron Radiation; Perfect Crystals, Mirrors And Multilayers," *Acta Crystallographia Section A*, June 1999, (BNL Number BNL-66248).
12. M. Born, E. Wolf, *Principles of optics*, 6th ed., Oxford ; New York : Pergamon Press, 1980.
13. H.W. Deckman, K.L. D'Amico, J.H. Dunsmuir, B.P. Flannery, S.M. Gruner, "Microtomography Detector Design: It's Not Just Resolution," *X-Ray Tomography, Imaging and Topography*, **641-651** (1998).
14. F.F. Hopkins, "High Res. Imaging with CT", *Proc. Indust. CTII, Trop. Conf., American Soc. Of NDT*, San Diago, (1991).
15. P.A. Rodnyi, Physical Processes in Inorganic Scintillators, CRC Press (1997).
16. C.L. Melcher and J.S. Schweitzer, *Nucl. Instr. and Meth.* **A314, 212** (1992).
17. P.A. Rodnyi, *Physical Processes in Inorganic Scintillators*, CRC Press, NY May (1997).
18. A. Evans, "The evaluation of medical images," *Medical Phy. Handbook 10*, Adam Hilger Ltd., Boston, (1981).
19. F. Natterer, *The Mathematics of Computerized Tomography*, Wiley (1986).
20. A. C. Kak, M. Slaney, *Principles of computerized tomographic imaging*, New York : IEEE Press (c1988).
21. A. Rosenfeld, A. Kak, *Digital Picture Processing*, San Diego: Academic Press (1982).
22. J.D. O'Sullivan, "A Fast Sinc Function Gridding Algorithm for Fourier Inversion in Computer Tomography", *IEEE Transactions on Medical Imaging* (Jan. 1985).
23. R.B. Marr, "Fast Filtered Back-Transform Reconstruction Algorithm for Generalized Fourier Data", *Soc. Of Magnetic Resonance in Med.*, 6th Annual Meeting (August 17-21, 1987).
24.] D. Slepian, H. O. Pollack. "Prolate Spheroidal Wave Functions, Fourier Analysis and Uncertainty - I", *The Bell System Technical Journal* (Jan. 1961).
25. A. L. Van Buren, "Tables of Angular Spheroidal Wave Functions", *Washington: Naval Research Laboratory* (1975).
26. R.K. Everett, P. Matic, D.P.I. Harvey, A. Kee, "The microstructure and mechanical response of porous polymers", *Materials Science And Engineering* A, **249: 1-2** (1998) pp. 7-13.